Sustainable Energy & Fuels

ROYAL SOCIETY OF CHEMISTRY

PAPER

Check for updates

Cite this: *Sustainable Energy Fuels*, 2024, **8**, 5906

Flexible laser-induced graphene-based electrodes modified with cobalt-manganese hexacyanoferrate as cathode materials for asymmetric supercapacitors†

Evgeniia Khairullina,*[ab] Alexandra Levshakova,[a] Maxim Fatkullin,[c] Maxim Tenevich,[d] Alexandr Shmalko,[e] Maxim Panov,[af] Alina Manshina,[a] Artem Lobinsky,[d] Raul D. Rodriguez[c] and Maria Kaneva*[d]

Received 19th July 2024
Accepted 7th November 2024

DOI: 10.1039/d4se00976b

rsc.li/sustainable-energy

The rapid progress in wearable electronics highlights the crucial need for advanced flexible energy storage solutions. This study presents a synergistic combination of laser-assisted polymer carbonization and ion deposition techniques to fabricate flexible electrode materials with outstanding electrochemical activity for energy storage applications. Flexible graphene-based electrodes fabricated through laser-assisted synthesis were modified with CoMnHCF nanocrystals using aqueous solutions of appropriate salts by a simple and environmentally friendly SILAR (Successive Ionic Layer Adsorption and Reaction) method. The CoMnHCF/laser-induced metal-polymer composite (LIMPc) electrode exhibited excellent electrochemical performance in an aqueous Na_2SO_4 electrolyte, achieving a high specific capacitance of 224.5 mF cm^{-2} (at 0.5 mF cm^{-2}). Furthermore, CoMnHCF/LIMPc showed remarkable rate capability and maintained long-term cycling stability after 10 000 cycles. A flexible asymmetric supercapacitor was assembled based on CoMnHCF/LIMPc as the cathode and LIMPc as the anode. This technique's versatility holds potential for fabricating other electrode materials with tailored compositions for diverse applications across multiple scientific and technological domains.

Introduction

The next generation of portable electronics demands the development of compact, flexible power sources with significant energy capacities. Supercapacitors are critical in closing the gap between conventional batteries and the dynamic requirements of modern, flexible electronics, including wearables, medical and implantable devices, and smart textiles.[1–4] Asymmetric supercapacitors (ASCs) are of particular interest because of their dual-mode energy storage: an electric double layer at the anode and faradaic processes at the cathode, merging the advantages of standard supercapacitors with those of lithium-ion batteries.[5–8]

Traditionally, ASCs cathodes are made from a variety of materials, including conductive polymers, carbon-based materials,[9–12] metal hydroxides,[13–16] and transition metal oxides.[17–22] Despite these advancements, the quest for new materials that offer a wider operational voltage window, extended lifetime, and cost-effectiveness continues relentlessly. In this context, Prussian blue analogs (PBAs) with the formula MHCF (where M = Co, Ni, Mn, Cu, Zn, *etc.*) emerge as promising electroactive materials to address these challenges.[23,24] The PBAs belong to the family of metal–organic frameworks (MOFs), which have an open three-dimensional structure with high surface area and controlled pore distribution. Their remarkable ability to transport guest molecules and facilitate cation intercalation, combined with excellent structural adaptability, positions them at the forefront of electrochemical applications. As a result, they exhibit outstanding electrochemical performance characterized by impressive specific

---

[a] *Institute of Chemistry, St. Petersburg State University, St. Petersburg 199034, Russia. E-mail: e.khayrullina@spbu.ru*

[b] *Department School of Physics and Engineering, ITMO University, St. Petersburg 191002, Russia*

[c] *Research School of Chemistry & Applied Biomedical Sciences, Tomsk Polytechnic University, Tomsk 634050, Russia*

[d] *Ioffe Institute, Hydrogen Energy Laboratory, St. Petersburg 194021, Russia. E-mail: skt94@bk.ru*

[e] *Nanotechnology Research and Education Centre RAS, Saint Petersburg Academic University, St. Petersburg 194021, Russia*

[f] *Center for physical Sciences and Information Technologies, St. Petersburg State Chemical Pharmaceutical University, St. Petersburg 197022, Russia*

† Electronic supplementary information (ESI) available: Photo of the LIMPc electrode, FACS and bending resistance of FASC. SEM images of LIMPc graphene-based electrode at various magnifications. X-ray photoelectron spectra of the N 1s. The possible chemical equations for redox processes in CoMnHCF. Impedance parameters obtained by data fitting with the electrical equivalent circuit and calculation. Characteristics of cathode materials and ASCs. Ragone plot of the CoMnHCF/LIMPc FASC compared with the reported supercapacitors. See DOI: **https://doi.org/10.1039/d4se00976b**

capacitance, rapid charge and discharge rates, and exceptional cyclic stability.[25] Among the various PBAs, cobalt hexacyanoferrate (CoHCF) exhibits a synergistic interaction between Co^{2+} and Fe^{2+} cations, resulting in remarkable values of both specific capacitance and cyclic stability, as demonstrated by numerous studies.[26–31] The performance of CoHCF-based materials has been extensively investigated in various applications such as electro- and photocatalysis,[32,33] metal-ion batteries,[34,35] and supercapacitors.[36,37]

Recent research has also highlighted the effectiveness of integrating PBAs with advanced carbon materials. These strategic combinations not only reduce the overall electrical resistance of the system, but also significantly improve the capacitive performance, paving the way for more efficient energy storage solutions.[38,39] Among the advanced carbon materials, laser-induced metal-polymer composite (LIMPc) exhibits unique robustness and sustainability in production due to its fabrication process, which is based on PET upcycling and an additive laser-assisted technique described in detail in ref. 23, 40 and 41. However, this approach faces issues in achieving optimal mass loading and even coating PBAs onto carbon electrode surfaces, as well as forming PBAs with nanostructured morphology, resulting in uneven surfaces. The use of the successive ionic layer adsorption and reaction (SILAR) technique to deposit CoMnHCF on LIMPc electrodes allows precise control of the deposition of nanostructures with required thickness.[42–44] This synthesis involves sequential processes of adsorption of cation- and anion-containing reagents from precursors, followed by interactions between ions through exchange or redox reactions. SILAR allows precise control and tuning over the material properties through varying precursor nature, solution composition, and substrate immersion time. Therefore, the proposed material design meets all the requirements for ASCs by providing excellent electrical conductivity and high specific capacity, along with important advantages over analogues, such as the excellent mechanical stability of LIMPc and the ability to precisely control the uniformity and loading of CoMnHCF.

This study presents a novel approach that combines laser-assisted polymer carbonization with the successive ionic layer adsorption and reaction (SILAR) method to fabricate flexible laser-induced graphene-based electrodes modified with cobalt-manganese hexacyanoferrate (CoMnHCF). Laser-assisted approaches offer unique advantages in creating advanced materials due to the special conditions provided by laser radiation.[45–53] Laser carbonization is used to synthesize laser-induced graphene/Al NPs/polymer composite (LIMPc) electrodes, which exhibit high electrical conductivity, remarkable durability, and mechanical resilience,[40] making this material promising for ASCs. As PET is a widely used polymer in various applications, this method was initially proposed as a means of converting PET waste into a functional material.[54] However, PET itself is not classified as a thermoset material due to its wide range of optical transparency. To overcome the transparency limitations of PET, the aluminium nanoparticles (AlNPs) were used as photothermal transducers to facilitate its pyrolysis. As a result, during pyrolysis, laser-induced integration of AlNPs into PET takes place with formation of graphene, resulting in a conductive laser-induced graphene/Al NPs/polymer composite film (Fig. 1). Furthermore, while LIG typically exhibits poor mechanical stability and is prone to delamination, the proposed method offers exceptional mechanical stability through a composite structure that retains its original properties even after rigorous sand abrasion tests.[40] Meanwhile, the SILAR process is employed for the first time to modify LIMPc with CoMnHCF nanocrystals, unlocking the full potential of LIMPc-based ASCs.

As a result, the CoMnHCF/LIMP electrodes demonstrated an excellent specific capacitance of 224.5 mF cm^{-2} at a current density of 0.5 mA cm^{-2} in a neutral 1 M Na_2SO_4 electrolyte. Furthermore, these electrodes exhibited excellent rate capability and cycling stability over 10 000 cycles. Our approach's strength lies in its versatility, allowing the development of diverse electrode materials. By fine-tuning the SILAR conditions, this approach can be tailored to fulfill the requirements across a broad range of scientific and technological applications.

Experimental section

Materials

Cobalt nitrate ($Co(NO_3)_2 \cdot 6H_2O$), manganese sulfate ($MnSO_4 \cdot 5H_2O$), potassium hexacyanoferrate(III) ($K_3[Fe(CN)_6]$), sodium sulfate (Na_2SO_4), sodium hydroxide (NaOH) were purchased from JSC LenReactiv (Saint Petersburg, Russia). All reagents were analytical grade and used without further purification. Aluminum nanoparticles (AlNPs) were purchased from Advanced Powder (Tomsk, Russia). Ultrapure Milli-Q water was used for all experiments (18.2 MΩ cm).

Graphene-based electrode fabrication

A detailed description of the flexible graphene-based electrode synthesis has been reported in previous work.[42] In summary, AlNP films were drop-casted onto a 0.7 mm thick polyethylene terephthalate sheet from an ethanolic dispersion with a 10 mg ml^{-1} concentration. Subsequently, upon drying, these films were subjected to laser-induced carbonization *via* a 450 nm pulsed laser diode (Fig. 1). After the irradiation, ultrasonication (120 W, 40 kHz) in distilled water was used to remove residues of poor integrated into laser-induced carbon network AlNPs. A low-pressure air plasma treatment with Zepto-BRS 200 (Diener electronic, Ebhausen, Germany) was used to improve the wettability of the graphene-based electrodes (air flow rate was 10 sccm). Incubation in a 1 M NaOH solution for 30 minutes at 60 °C was performed to dissolve the residual aluminum-based nanoparticles present on the surface.[41] The synthesized flexible graphene-based electrodes were denoted as LIMPc (Laser-Induced Metal-Polymer composite). The dimensions of the working part of the LIMPc electrode were 6 mm by 8 mm excluding the holder (Fig. S1a†).

Modification of LIMPc electrodes with cobalt-manganese hexacyanoferrate using the SILAR method

Preparation of CoMnHCF was carried out on a graphene-based electrode using the SILAR method. The formation process

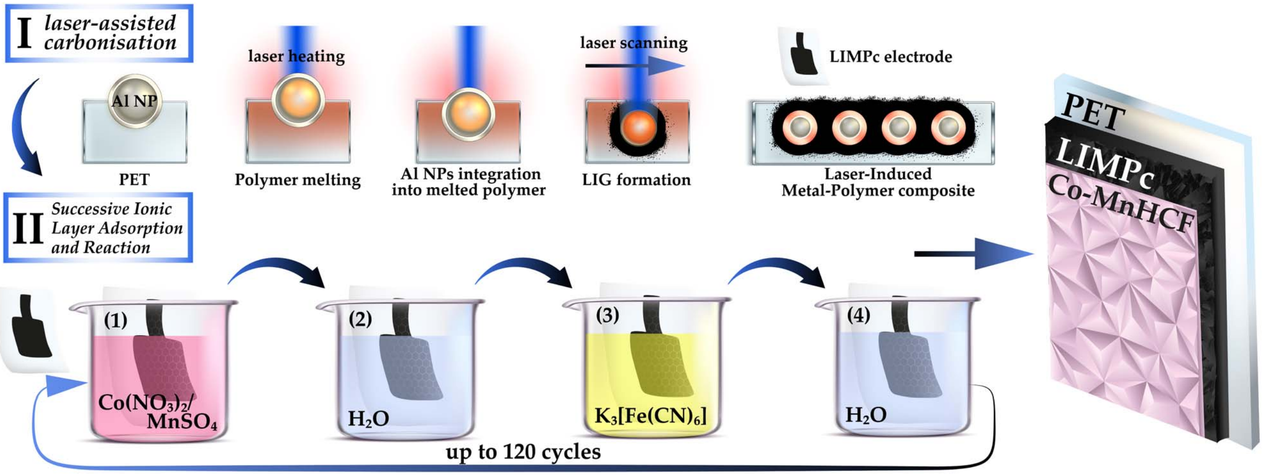

Fig. 1 Scheme of LIMPc electrode formation and further modification by Co-MnHCF.

included several successive stages of treating the LIMPc substrate (Fig. 1). Parameters such as processing time and concentration of the precursor solutions were determined based on a series of preliminary experiments. The cationic precursor was a mixture of 0.01 $Co(NO_3)_2$ and 0.01 M $MnSO_4$ solution, and a 0.01 M $K_3[Fe(CN)_6]$ solution was used as the anionic precursor. In the first stage, the LIMPc electrode was immersed in the cationic precursor for 15 s. After that, the reagent excess was removed by rinsing the substrate with deionized water. Further in the second stage, the LIMPc electrode was immersed in the anionic precursor for 15 s, and the excess reagent was removed again by rinsing the electrode with deionized water for 30 s. Thus, first, the adsorption of cobalt and manganese cations occurs, then the reaction between adsorbed Co^{2+} and Mn^{2+} cations and adsorbed $[Fe(CN)_6]^{3-}$ anions led to the formation of a CoMnHCF. The number of SILAR treatment cycles was varied from 30 to 120 times. After SILAR synthesis, the CoMnHCF/LIMPc electrode was air-dried at an ambient temperature. For comparative analysis, cobalt and manganese hexacyanoferrates (CoHCF and MnHCF) were also synthesized under similar conditions, but a solution of only one salt ($Co(NO_3)_2$ or $MnSO_4$) was used as the cationic precursor.

Flexible asymmetric supercapacitors (FASC) assembly

The flexible device was assembled using PVA/Na_2SO_4 gel electrolyte. For preparation of PVA/Na_2SO_4 gel electrolyte 1 g PVA was added into 25 ml deionized water. Firstly, solution PVA in water placed on water bath and stirred at 95 °C for 1 h using a thermostatic magnetic stirrer and cooled down to room temperature. On the second stage 5 ml 0.5 M Na_2SO_4 solution was added to PVA solution and intensely stirred. Finally, the solution was then stood still on air for 24 hours to obtain Na_2SO_4 gel. The flexible device was assembled using PVA/Na_2SO_4 gel electrolyte. CoMnHCF_90/LIMPc and LIMPc were used as cathode and anode, respectively. Further, both LIMPc and CoMnHCF_90/LIMPc electrodes were dipped in the PVA–Na_2SO_4 gel electrolyte and assembled to form an FASC with cellulose paper as the separator between them. Finally, the flexible device was obtained by packaging using a polyimide film (Fig. S1b†).

Characterization techniques

X-ray diffraction (XRD) analysis was performed with a Bruker D2 Phaser diffractometer equipped with a LynxEye detector (Bruker-AXS, Karlsruhe, Germany) to establish the phase composition. Raman spectroscopy was carried out using a confocal spectrometer Senterra (Bruker, Billerica, MA, USA). The Raman spectra were acquired with a 532 nm solid-state laser at 10 mW power using a 50× objective and were collected two times. X-ray photoelectron spectroscopy (XPS) was performed using an ESCALAB 250Xi electron spectrometer (ThermoFisher Scientific, Waltham, MA, USA). The morphology and elemental analysis of the electrode were investigated by scanning electron microscopy (SEM) on a Zeiss Merlin (Karl Zeiss, Oberkochen, Germany) equipped with a field emission cathode, a GEMINI-II electron-optics column, and an INCAx-act energy dispersive X-ray spectrometer (EDX) (Oxford Instruments, Abingdon, UK).

Electrochemical measurements

The electrochemical performance of the electrode was investigated with a standard three-electrode cell using Corrtest CS300 potentiostat (Wuhan CorrTest co. LTD., Wuhan, China) at room temperature. The reference and counter electrodes were an Ag/AgCl (3.5 M KCl) and a carbon rod, respectively. The geometric area of the working electrode was fixed and reached 0.48 cm^2. Sodium sulfate solution (1 M Na_2SO_4) was used as a supporting electrolyte for electrochemical measurements. Cyclic voltammetry (CV) measurements were obtained in the potential windows from 0.0 V to 1.3 V (*vs.* Ag/AgCl) at different scan rates (5–50 mV s^{-1}). Galvanostatic charge–discharge (GCD) measurements were obtained at various current densities (0.25–4 mA cm^{-2}). The specific areal capacitance (C, mF cm^{-2}) of the prepared electrode was calculated from the GCD measurements using eqn (1):

$$C = \frac{I \times \mathrm{d}t}{S \times \mathrm{d}V}, \tag{1}$$

where I is the applied current (mA), dt is the discharge time (s), dV is the potential window (V) and S is the area of the electrode (cm^2).[55,56]

The areal energy density (E_A, μW h cm^{-2}) and areal power density (P_A, μW cm^{-2}) of supercapacitors were calculated based on the following eqn (2) and (3):

$$E = \frac{C \times (\Delta V^2)}{2 \times 3.6}, \tag{2}$$

$$P = 3600 \times \frac{E}{\Delta t}, \tag{3}$$

where ΔV is the operating potential window (V) of supercapacitors, Δt is the discharge time (s).[57,58]

Electrochemical Impedance Spectroscopy (EIS) measurements were conducted over a frequency range of 0.01 Hz to 10 kHz with an amplitude of 10 mV at open circuit voltage. The EIS results were analyzed using the EIS Spectrum Analyser software for equivalent circuit simulation and calculation of the electrochemical parameters of the system. Phase angle was calculated by eqn (4):

$$\varnothing = -\tan^{-1}\frac{Z'}{Z''}, \tag{4}$$

where Z' and Z'' are the real and imaginary components of impedance, respectively.[59]

Results and discussion

The laser-induced graphene/Al NPs/polyethylene terephthalate (PET) composite was synthesized through laser-assisted integration of nanoparticles into the PET surface. This advanced graphene-based nanocomposite exhibits high electrical conductivity and exceptional toughness due to the formation of an Al–Al_2O_3–Al_4C_3–graphene network within the polymer matrix, as reported in a previous study.[40] This graphene-based composite displays remarkable mechanical resistance, as well as structural and chemical stability, when exposed to various solvents, making it a promising candidate for a range of electrochemical applications, including capacitors. To fully demonstrate the potential of the graphene-based electrodes with their superior mechanical properties, the electrodes were pretreated with a 1 M NaOH solution before SILAR synthesis. This step aimed to dissolve Al-based impurities on the electrode surface, which formed during synthesis, thereby unblocking all active sites while preserving the composite's integrity.

Structure and morphology of CoHCF, MnHCF and CoMnHCF

Scanning electron microscopy (SEM) images of LIMPc electrodes modified with CoHCF, MnHCF, and CoMnHCF at various magnifications are shown in Fig. 2a–c. It was previously reported that the initial graphene-based electrode is characterized by high roughness and well-developed morphology (Fig. S2†). These surface characteristics make the modified LIMPc electrode a prospective substrate for ion deposition due to its large surface area along with its remarkable mechanical and electrical properties. The CoHCF deposition on the LIMPc electrode surface under SILAR conditions results in the formation of nanoparticles that form spherical agglomerates with a size of up to 80 nm (Fig. 2a). CoHCF growth likely initiates from individual nucleation sites, leading to the formation of discrete spherical agglomerates. Incorporating manganese ions into the CoHCF lattice significantly affects the morphology and promotes the development of cubic nanocrystals, which gradually grow together (Fig. 2c). At the same time SILAR using only manganese salt solution under similar conditions does not lead to the formation of bulk cubic crystals (Fig. 2b). EDX analysis of all samples revealed the presence of Co, Fe, K, N, and C within the composition of the nanocrystals (Fig. 2d and e). The CoMnHCF and MnHCF samples additionally contained Mn. Based on the quantitative assessment, the empirical formula for the CoHCF sample was determined to be $K_{0.49}Co_{2.86}[Fe(CN)_6]_2$, corresponding to the elemental ratio of K : Co : Fe : N at 1.6 : 9.3 : 6.5 : 38.6, respectively. For the CoMnHCF sample, the derived formula was $K_{0.41}Co_{2.57}Mn_{0.36}[Fe(CN)_6]_2$, with an EDX elemental ratio of K : Co : Mn : Fe : N at 1.7 : 10.7 : 1.5 : 8.3 : 51.0. Element mapping results indicate a homogeneous distribution of all elements within the CoMnHCF nanocrystals.

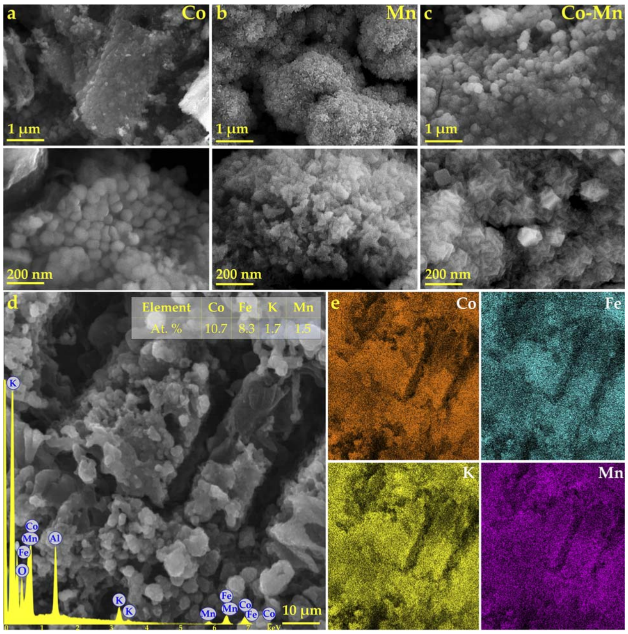

Fig. 2 SEM images (a) CoHCF, (b) MnHCF, (c and d) CoMnHCF synthesized after 90 SILAR cycles on graphene-based electrodes, and (e) EDX elemental mapping images of CoMnHCF.

Further investigation into the effect of SILAR cycles' count on the morphological characteristics of CoMnHCF was judged a crucial step, given its demonstrated potential among the studied hexacyanoferrates, as evidenced by SEM images.

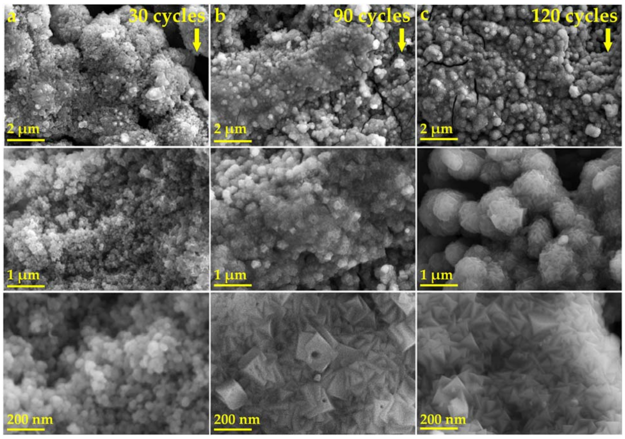

Fig. 3 SEM images of CoMnHCF synthesized after (a) 30, (b) 90 and (c) 120 SILAR cycles on graphene-based substrate.

Increasing the SILAR cycles leads to the size increase of crystal facets (Fig. 3a–c). Notably, after 120 SILAR cycles, a significant coalescence of cubic nanocrystals was observed, leading predominantly to the retention of a single cube corner on the surface, accompanied by a decrease in surface area.

The Raman spectra (Fig. 4a) and X-ray diffraction patterns (Fig. 4b) results were used to analyze the phase composition of hexacyanoferrates and identify potential lattice changes resulting from Mn^{2+} incorporation. Notably, the 90 cycles of SILAR resulted in the formation of an XRD-inactive layer of MnHCF, in contrast to cobalt manganese hexacyanoferrate and cobalt hexacyanoferrate, which exhibit the expected reflections characteristic of the Prussian blue analogue (PBA) phase. The diffraction peaks for CoHCF at 2θ values of 17.3°, 24.5°, 34.9°, and 39.2° correspond to the characteristic (200), (220), (400), and (420) planes indicative of face-centered cubic structures (JCPDS no. 46-0907), similar to other Prussian blue analogs.[60–62] In addition, we have included the XRD pattern of physical mixture samples synthesized with 90 SILAR cycles, consisting of 45 cycles of MnHCF and 45 cycles of CoHCF. The XRD pattern of this physical mixture corresponds to that of CoHCF. At the same time, a subtle shift to lower angles in the 2θ values of CoMnHCF was noted compared to CoHCF (Fig. 4b, inset). Such minor alteration in the diffraction angles suggests that the SILAR synthesis technique likely leads to Co and Mn integrating within the same crystal lattice rather than simply forming a physical mixture of CoHCF and MnHCF.[63] This is consistent with previous findings of analogous structural substitutions in mixed-metal hexacyanoferrates.[64] Additional peaks in the XRD pattern, around 26.1°, 44.4°, and 53.5°, may be assigned to the graphite and graphene reflections from the carbon electrode.[65–67] XRD characterization revealed no structural differences between CoHCF and CoMnHCF, which is supported by the Raman spectroscopy data (Fig. 4a). The number of peaks is preserved upon the introduction of Mn^{2+}, indicating the absence of secondary manganese-related phases. The peaks shifts, due to the replacement of cobalt by manganese, supports that the structure of CoMnHCF is maintained as in CoHCF. Furthermore, the Raman spectra of CoMnHCF exhibited bands in the range of 2000–2300 cm^{-1}, corresponding to the stretching vibrations $Fe^{3+}–C{\equiv}N–Co^{2+}$ (ref. 68) and $Fe^{3+}–C{\equiv}N–Mn^{2+}$.[69] Bands in the 600–700 cm^{-1} range are related to Fe–C stretching

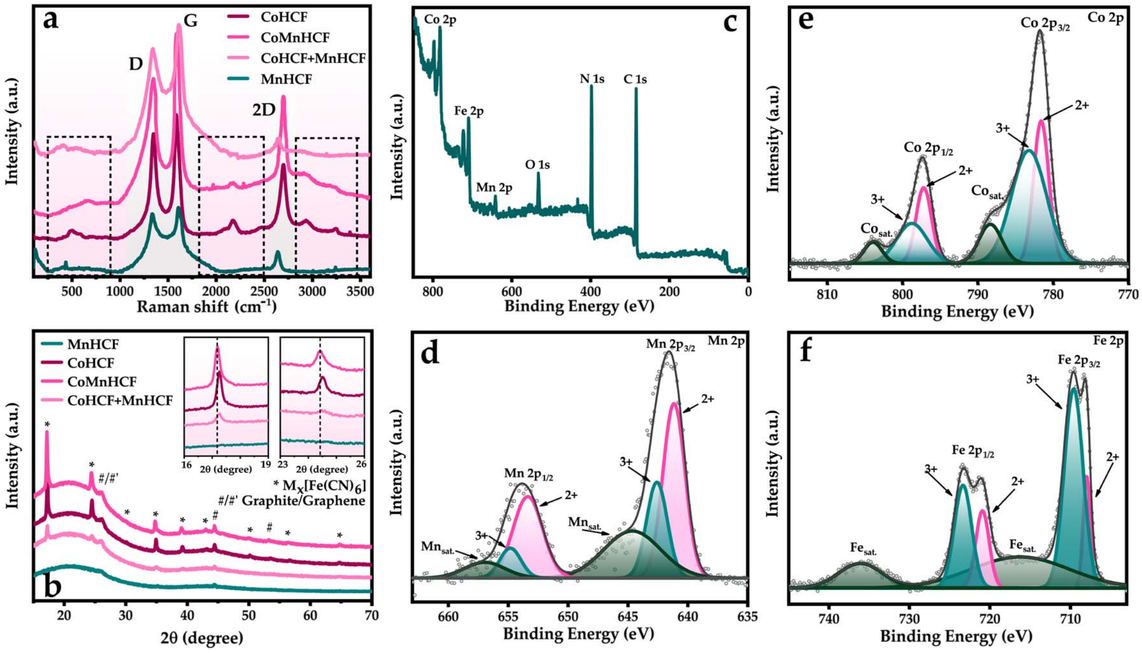

Fig. 4 (a) Raman spectra of MnHCF, CoHCF, CoMnHCF and CoHCF + MnHCF synthesized after 90 cycles on graphene-based substrate (pink regions contain MnHCF, CoHCF and CoMnHCF bands, gray regions contain graphene bands) and (b) XRD patterns. (c) Survey X-ray photoelectron spectra and XPS spectra of the Mn 2p (d), Co 2p (e) and Fe 2p (f) regions of CoMnHCF synthesized after 90 cycles on the LIMPc electrode.

vibrations, while those around 480 cm^{-1} are attributed to Co–N bending vibrations.[34] Alongside the analysis of CoMnHCF nanocrystals, Raman spectroscopy proves to be an invaluable tool for characterizing carbon nanomaterials. The Raman spectra provide robust evidence of graphene formation, as indicated by the D, G, and 2D fingerprint peaks at 1346, 1587, and 2699 cm^{-1}, respectively.[70]

The elemental composition and chemical states of the CoMnHCF nanocrystals were thoroughly investigated using XPS. This analysis confirmed the presence of Co, Mn, Fe, C, O, K, and N (Fig. 4c), which is consistent with the EDX results. The XPS spectrum of the N 1s can be deconvolved into two different peaks (Fig. S3†). The peak observed at lower binding energies is attributed to nitrogen in cyano groups coordinated with the transition metals in CoMnHCF.[70] In turn, the peak at higher binding energies is likely associated with nitrogen in the form of imine or amide.[71] Deconvolution of the high-resolution Co 2p XPS spectra of CoMnHCF revealed two spin–orbit doublets arising from $2p_{3/2}$ and $2p_{1/2}$ at 781.7 and 797.4 eV, respectively (Fig. 4e). The Co $2p_{3/2}$ peak was fitted with two components at 781.2 eV for Co^{2+} and 783.2 eV for Co^{3+}, while the Co $2p_{1/2}$ peak was deconvoluted into 797.2 eV for Co^{2+} and 798.2 eV for Co^{3+} components.[72,73] As illustrated in Fig. 4d, the Mn 2p could be deconvoluted into pairs of peaks for Mn $2p_{3/2}$ and Mn $2p_{1/2}$. The peaks at 641.2 eV for Mn^{2+} $2p_{3/2}$ and 642.6 eV for Mn^{3+} $2p_{3/2}$, along with peaks at 653.5 eV for Mn^{2+} $2p_{1/2}$ and 654.9 eV for Mn^{3+} $2p_{1/2}$, were observed. Fig. 4f also presents the Fe 2p XPS spectrum, showing two deconvoluted peaks for $2p_{3/2}$ at 708.0 eV for Fe^{2+} and 709.6 eV for Fe^{3+}, and two for $2p_{1/2}$ at 720.9 eV for Fe^{2+} and 723.4 eV for Fe^{3+}.[72,74] The large satellite peak at Fe 2p spectra can indicate significant charge transfer from the ligand (C≡N group) to the metal (Fe).[75] Furthermore, the Pauling electronegativity of the metal (M) is an essential parameter for understanding the electron density distribution in MHCFs. The charge transfer from the C≡N group to iron decreases as the electron density shifts to the other metal. Since cobalt has a moderate Pauling electronegativity comparable to that of iron, while manganese has a even lower electronegativity, the ligand-to-metal charge transfer (LMCT) from the C≡N group to Fe is reasonable and results in the appearance of satellite peaks. Our founding confirm the simultaneous presence of different oxidation states of cations during the formation of MHCF, as has been observed in a number of studies.[60,72,74] In particular, it has been demonstrated that Fe^{2+} and Fe^{3+}, as well as Co^{2+} and Co^{3+}, coexist within CoHCF.[72,76,77] Moreover, it is known that the microstructure of MnHCF undergoes a transformation due to the transition from Fe^{3+}–CN–Mn^{2+} to Fe^{2+}–CN–Mn^{3+}.[74,78–80]

Electrochemical measurements

The electrochemical characteristics of CoHCF/LIMPc, MnHCF/LIMPc, and CoMnHCF/LIMPc as a flexible cathode in supercapacitors were studied by the cycling voltammetry (CV) and galvanostatic charge–discharge (GCD) techniques (Fig. 5) The measurements were carried out in an aqueous solution of 1 M Na_2SO_4. Fig. 5a shows the CV curves of LIMPc, CoHCF/LIMPc, MnHCF/LIMPc, and CoMnHCF/LIMPc electrodes at a scan rate of 20 mV s^{-1}. The prominent redox peaks are observed in the modified flexible graphene-based electrodes, reflecting a pseudocapacitive nature of the electrode material. The redox behavior of hexacyanoferrates, including CoHCF, MnHCF, and CoMnHCF, has been widely discussed in the literature.[63,81,82] CoMnHCF consists of three metal ions (Co, Mn, Fe), each capable of participating in redox reactions. The redox transitions for cobalt (Co^{3+} to Co^{2+}) and manganese (Mn^{3+} to Mn^{2+}) have close potentials and can be clearly observed in MnHCF and CoHCF, but these transitions become indiscernible when present in CoMnHCF. Furthermore, while the electrochemical signals for the iron redox couple (Fe^{3+} to Fe^{2+}) can be clearly distinguished in MnHCF, they merge into a broad peak within the CoMnHCF CV curve. The possible chemical equations for these redox processes can be found in the ESI (Scheme S1†).[83,84]

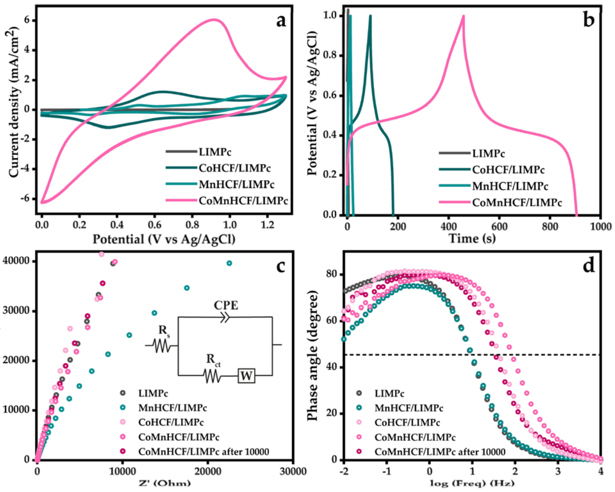

Fig. 5 (a) CV curves at a scan rate of 20 mV s^{-1}, (b) GCD curves at 0.5 mA cm^{-2}, (c) Nyquist plots. Inset: equivalent circuit model used to fit the experimental EIS data and (d) Bode phase plots of LIMPc, CoHCF/LIMPc, MnHCF/LIMPc and CoMnHCF/LIMPc electrodes obtained by 90 SILAR cycles.

Compared to the CoHCF/LIMPc and MnHCF/LIMPc electrodes, the CV curves of the CoMnHCF/LIMPc show a much higher peak current, indicating the positive effect of the simultaneous presence of cobalt and manganese ions within the hexacyanoferrate lattice on its electrochemical performance.

The charge–discharge curve profiles are shown in Fig. 5b. The nonlinear shape of the curves indicates the pseudocapacitive properties of the electrodes. The specific areal capacitance values calculated from the charge–discharge curves at a current density of 0.5 mA cm^{-2} (Fig. 5b) for CoHCF/LIMPc, MnHCF/LIMPc, and CoMnHCF/LIMPc electrodes were 44.3, 6.45, and 224.5 mF cm^{-2}, respectively. These values are significantly higher than those of the initial LIMPc electrode (1.3 mF cm^{-2} in Na_2SO_4 and 4.3 mF cm^{-2} in KCl[40]).

The EIS analysis (Fig. 5c and d) was carried out to gain further insight into the interfacial electrochemistry and charge transfer kinetics at the electrode–electrolyte interface of the fabricated electrodes. The equivalent circuit model includes parameters for solution resistance (R_S) and charge transfer resistance (R_{CT}). The constant phase element (CPE) accounts for the behavior of the double layer capacitance, while W is the Warburg impedance characterizing the diffusion process.

As can be seen from the Nyquist plot (Fig. 5c), the charge transfer resistance (R_{CT}) is minimal in the high frequency range and shows no sign of a semicircle. This observation is supported by the results of equivalent circuit modeling, which provided calculated E_{CT} values (Fig. 5c, inset). Notably, the CoMnHCF electrodes exhibited lower R_S (7.4 Ω) and R_{CT} (1.7 Ω) values compared to the LIMP, CoHCF and MnHCF electrodes (Table S1†).

The kinetics associated with charge storage can be analysed using the Bode plot (Fig. 5d). The phase angle typically indicates a purely resistive behavior at 0°, a capacitive response at −90° and a diffusion limited response at −45°.[59] In the case of the LIMPc electrode, a phase angle of −72° was observed at a low frequency of 10 mHz, indicating the near ideal capacitive nature of the electrode.[85,86] In contrast, the MnHCF, CoHCF and CoMnHCF electrodes showed a decrease in phase angle to values between −52° and −64°, highlighting the role of pseudocapacitance in these materials.[85]

The frequency at which the phase angle reaches −45° is identified as the crossover frequency,[59] which marks the transition between capacitive and resistive behavior, as indicated by a horizontal dashed line in Fig. 5d. For the LIMPc electrode, this crossover frequency occurs at 9.77 Hz, indicating that the resistive component predominates for charging times shorter than 0.1 s (with the relaxation time constant estimated to be $\tau_0 = 1/f_0$).[86] Conversely, for the CoMnHCF electrode, the crossover frequency at 87.1 Hz is significantly higher (9 times) than that of the LIMPc, indicating that capacitive processes remain active on time scales around 0.011 seconds.

Influence of the number of SILAR cycles on electrochemical characteristics

A series of the LIMPc electrodes modified with CoMnHCF by 30-120 SILAR cycles was investigated (Fig. 6a and b) to assess the impact of the number of cycles on the electrochemical performance. The specific areal capacitance increased from 31.8 mF cm^{-2} to 246.7 mF cm^{-2} at a current density of 0.5 mA cm^{-2}, correlating with the rise in the number of SILAR cycles. Notably, capacitive properties showed significant enhancement up to 90 cycles, but additional increases in SILAR cycles resulted in negligible changes, likely due to the formation of an excessively thick hexacyanoferrate layer. Consequently, the CoMnHCF_90/LIMPc electrode was selected as the optimal electrode for more detailed electrochemical studies, considering a balance between optimal performance, material economy, and manufacturing time.

The GCD curves (Fig. 6c) of the CoMnHCF_90/LIMPc electrode were recorded over a range of current densities from 0.25 to 4 mA cm^{-2}. From these discharge curves, specific areal capacitance values of 237.2, 224.5, 168.7, 137.6 and 112.7 mF cm^{-2} were calculated at current densities of 0.25, 0.50, 1, 2 and 4 mA cm^{-2}, respectively.

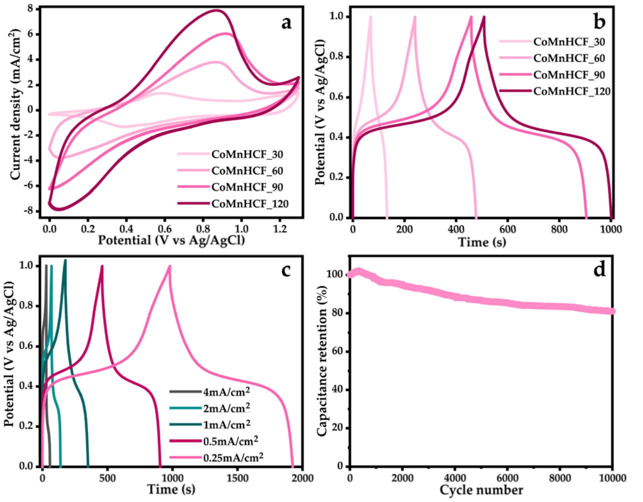

Fig. 6 (a) CV curves at 20 mV s^{-1} and (b) GCD curves at 0.5 mA cm^{-2} of CoMnHCF/LIMPc electrodes synthesized after 30–120 SILAR cycles, (c) specific areal capacitance at different current densities of the CoMnHCF_90/LIMPc and (d) long-term cyclic stability plot of the CoMnHCF_90/LIMPc electrode.

Moreover, the CoMnHCF_90/LIMPc electrode revealed exceptional long-term cycling stability, preserving 80% of its initial capacity after 10 000 charge/discharge cycles (Fig. 6d). The electrode was analyzed using electrochemical impedance spectroscopy (EIS) following extended stability tests. According to the Nyquist plot and subsequent calculations, the resistivity values of R_s and R_{CT} have shown a slight increase compared to the original sample, with R_s rising from 7.4 Ω to 8.75 Ω and R_{CT} from 1.7 Ω to 22.3 Ω (Table S1†). Additionally, a decrease in the crossover frequency at a phase angle of 45° was observed, accompanied by a corresponding increase in the relaxation time constant (Fig. 5d). These changes are likely attributable to the depletion of the near-electrode layer and the emergence of diffusion limitations. In comparison with other advanced flexible electrode materials listed in Table S2,† the CoMnHCF_90/LIMPc cathode developed in this study demonstrates good electrochemical performance.

Flexible asymmetric supercapacitors assembly

A test assembly of the FASC was carried out using CoMnHCF_90/LIMPc as cathode and LIMPc as anode (Fig. S1b†). Fig. 7a shows the CV curves of the LIMPc and CoMnHCF/LIMPc electrodes at a scan rate of 20 mV s^{-1}. The LIMPc electrode works in the potential window from −0.9 to 0 V, while the CoMnHCF/LIMPc electrode works from −0 to 1.3 V. These two potential ranges suggest the possibility of developing an asymmetrical device with extended cell voltages more than 1.2 V.[87] An important factor in the development of such devices is to evaluate the capacitance matching to optimize the electrochemical performance of FASCs. During the device's operation, the charges stored in the positive and negative electrodes must remain equal. A typical method to achieve capacity matching involves balancing the mass loading

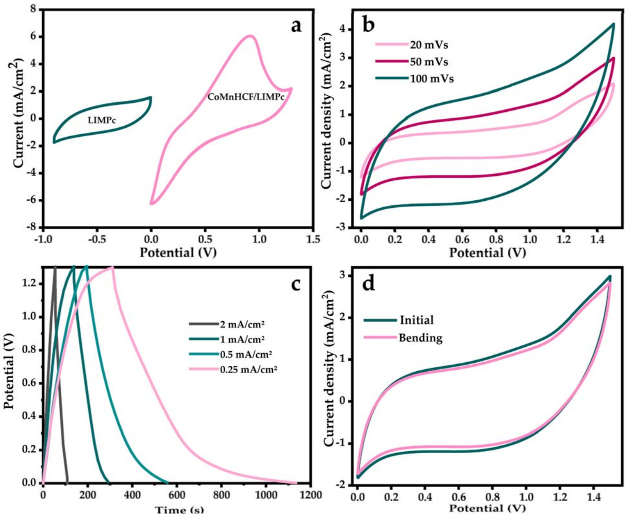

Fig. 7 (a) CV curves of LIMPc and CoMnHCF_90/LIMPc electrodes, (b) CV curves of FASC at different scan rate, (c) charge–discharge curves of FASC at different current density and (d) CV curves of FASC in the normal and bending states.

of the positive and negative electrodes ($q^+ = q^-$).[57] As numerous studies have shown, the direct assessment of mass loading and specific gravimetric capacity of active materials in flexible electrodes within a planar configuration is a significant challenge.[57] In our case, it is difficult to measure the mass load for the LIMPc electrode due to the peculiarities of the laser-induced carbonization process. Based on the charge balance equation ($q^+ = q^-$), the balance the areal capacitance of the positive and negative electrodes in FASC can be expressed by the following equation: $C_{A-}V_{A-}A_- = C_{A+}V_{A+}A_+$, where C, V and A are the areal capacitance, potential ranges and the area of the electrodes. Considering that A_+ and A_- are equal in the configuration of our system, then the equation can be written as: $C_{A-}V_{A-} = C_{A+}V_{A+}$. The calculation results showed that the ratio (q^-/q^+) is 0.4.

The cyclic voltammograms of the designed FASC were recorded with a different scan rate from 20 to 100 mV s^{-1} at voltage windows of 0–1.5 V inferring a good capacitive behavior and rate capability (Fig. 7b). The GCD curves obtained at a different current density from 0.25 to 2 mA cm^{-2} indicates that the device has good charge–discharge capability until 1.3 V (Fig. 7c). The FASC showed a maximum areal specific capacitance of 158.3 mF cm^{-2} at a current density of 0.25 mA cm^{-2}. In addition, the bending test of the device showed good resistance (Fig. 7d).

The FASC exhibited a maximum areal energy density of 44.5 μW h cm^{-2} and a maximum areal power density of 184.0 mW cm^{-2}. A comparison with other advanced flexible electrode materials is presented in the form of a Ragone plot, as shown in Fig. S4.† The synthesized FASC occupies a promising position among the analogs considered. Despite the presence of ASCs with superior performance in terms of capacity, the developed composite exhibits impressive properties, including stability in bending tests and mechanical robustness of the carbon support as well as flexibility and sustainability in manufacturing. Future directions for this work could include the development of microcapacitors[57,85,88] based on the results presented here to further advance the field.

Conclusions

We have successfully engineered a flexible graphene-based electrode, modified with cobalt-manganese hexacyanoferrate through a synergistic approach combining laser-assisted polymer carbonization and ion deposition techniques. The seamless integration of an homogeneous single-phase mixed-metal Prussian Blue Analog (PBA) across the electrode's surface was confirmed by EDX, XRD, Raman, and XPS analysis techniques. The strategic introduction of manganese ions into the CoHCF structure has been found to catalyze the growth of cubic CoMnHCF nanocrystals, significantly enhancing the electrode's electrochemical properties. In an aqueous Na_2SO_4 electrolyte, the CoMnHCF-modified graphene electrode demonstrated exceptional electrochemical performance, achieving a high specific capacitance of 224.5 mF cm^{-2} at a scan rate of 0.5 mA cm^{-2}. Furthermore, the electrode exhibited excellent long-term cycling stability, maintaining its performance after 10 000 charge/discharge cycles. These results indicate that the material holds considerable promise as a cathode for flexible asymmetric supercapacitors.

Data availability

The data supporting this article have been included as part of the ESI.†

Author contributions

Conceptualization, A. A. L., E. K., M. K. and A. L.; methodology, M. F., M. K., A. L. and E. K.; validation, M. F., M. K., A. L. and E. K.; formal analysis, M. K., A. L., E. K. and A. A. L.; investigation, A. L., M. K. and E. K.; resources, M. T., A. S.; data curation, E. K., M. K. and A. L.; writing—original draft preparation, M. K., A. L. and E. K.; writing—review and editing, M. K., E. K., A. L., I. T., A. M., M. P., R. R. and A. A. L.; visualization, A. L., E. K. and M. K.; supervision, R. R, A. M., M. K., E. K. and A. A. L.; project administration, M. K., A. L. and E. K.; funding acquisition, M. K. All authors have read and agreed to the published version of the manuscript.

Conflicts of interest

The authors declare no conflict of interest.

Acknowledgements

This research was funded by the Russian Science Foundation (grant 24-29-00758). **https://rscf.ru/en/project/24-29-00758/**. The authors would also like to thank the SPBU Research Park, especially the Nanotechnology Interdisciplinary Centre, the Centre for Physical Methods of Surface Investigation, the

Centre for X-ray Diffraction Studies, and the Centre for Optical and Laser Materials Research.

Notes and references

1 A. Lipovka, M. Fatkullin, S. Shchadenko, I. Petrov, A. Chernova, E. Plotnikov, V. Menzelintsev, S. Li, L. Qiu, C. Cheng, R. D. Rodriguez and E. Sheremet, *ACS Appl. Mater. Interfaces*, 2023, **15**(32), 38946–38955, DOI: 10.1021/acsami.3c06968.

2 E. Abyzova, E. Dogadina, R. D. Rodriguez, I. Petrov, Y. Kolesnikova, M. Zhou, C. Liu and E. Sheremet, *Mater. Today Bio*, 2023, **22**, 100784, DOI: 10.1016/j.mtbio.2023.100784.

3 S. S. Nardekar and S. J. Kim, *Adv. Sci.*, 2023, **10**(28), 2303918, DOI: 10.1002/advs.202303918.

4 S. Manoharan, K. Krishnamoorthy, V. K. Mariappan, D. Kesavan and S. J. Kim, *Chem. Eng. J.*, 2021, **421**(1), 129548, DOI: 10.1016/j.cej.2021.129548.

5 Y. Shao, M. F. El-Kady, J. Sun, Y. Li, Q. Zhang, M. Zhu, H. Wang, B. Dunn and R. B. Kaner, *Chem. Rev.*, 2018, **118**, 9233–9280, DOI: 10.1021/acs.chemrev.8b00252.

6 N. Wu, X. Bai, D. Pan, B. Dong, R. Wei, N. Naik, R. R. Patil and Z. Guo, *Adv. Mater. Interfaces*, 2021, **8**(1), 2001710, DOI: 10.1002/admi.202001710.

7 K. S. Poonam, A. Arora and S. K. Tripathi, *J. Energy Storage*, 2019, **21**, 801–825, DOI: 10.1016/j.est.2019.01.010.

8 J. Li, Q. Jiang, N. Yuan and J. Tang, *Materials*, 2018, **11**(11), 2280, DOI: 10.3390/ma11112280.

9 Z. Zhai, L. Zhang, T. Du, B. Ren, Y. Xu, S. Wang, J. Miao and Z. Liu, *Mater. Des.*, 2022, **221**, 111017, DOI: 10.1016/j.matdes.2022.111017.

10 Y. Wang, L. Zhang, H. Hou, W. Xu, G. Duan, S. He, K. Liu and S. Jiang, *J. Mater. Sci.*, 2021, **56**(2), 173–200, DOI: 10.1007/s10853-020-05157-6.

11 L. Miao, Z. Song, D. Zhu, L. Li, L. Gan and M. Liu, *Mater. Adv.*, 2020, **1**, 945–966, DOI: 10.1039/D0MA00384K.

12 A. G. Olabi, Q. Abbas, M. A. Abdelkareem, A. H. Alami, M. Mirzaeian and E. T. Sayed, *Batteries*, 2023, **9**(1), 19, DOI: 10.3390/batteries9010019.

13 G. Wang, L. He, Z. Guo and M. Li, *J. Energy Storage*, 2023, **72**(C), 108544, DOI: 10.1016/j.est.2023.108544.

14 X. Li, J. Ren, D. Sridhar, B. Bin Xu, H. Algadi, Z. M. El-Bahy, Y. Ma, T. Li and Z. Guo, *Mater. Chem. Front.*, 2023, **7**, 1520–1561, DOI: 10.1039/D2QM01346K.

15 S. Naeem, A. V. Patil, A. V. Shaikh, U. P. Shinde, D. Husain, M. T. Alam, M. Sharma, K. Tewari, S. Ahmad, A. A. Shah, S. A. Ali and A. Ahmad, *Adv. Mater. Sci. Eng.*, 2023, **2023**(1), 1133559, DOI: 10.1155/2023/1133559.

16 A. L. Brisse, P. Stevens, G. Toussaint, O. Crosnier and T. Brousse, *Materials*, 2018, **11**(7), 1178, DOI: 10.3390/ma11071178.

17 I. Melkiyur, Y. Rathinam, P. S. Kumar, A. Sankaiya, S. Pitchaiya, R. Ganesan and D. Velauthapillai, *Renew. Sustain. Energy Rev.*, 2023, **173**, 113106, DOI: 10.1016/j.rser.2022.113106.

18 C. An, Y. Zhang, H. Guo and Y. Wang, *Nanoscale Adv.*, 2019, **1**, 4644–4658, DOI: 10.1039/C9NA00543A.

19 Y. Liu, D. Luo, K. Shi, X. Michaud and I. Zhitomirsky, *Nano-Struct. Nano-Objects*, 2018, **15**, 98–106, DOI: 10.1016/j.nanoso.2017.08.010.

20 A. K. Lichchhavi, P. M. Shirage and A. Kanwade, *J. Energy Storage*, 2022, **55**(C), 105692, DOI: 10.1016/j.est.2022.105692.

21 M. S. Mohamed Saleem, R. Swaminathan, V. Mohan, N. U. H. Liyakath Ali and S. J. Kim, *J. Ind. Eng. Chem.*, 2024, **136**, 493–500, DOI: 10.1016/j.jiec.2024.02.038.

22 R. Swaminathan, P. Pazhamalai, K. Krishnamoorthy, V. Natraj, V. Krishnan and S. J. Kim, *J. Energy Storage*, 2024, **83**, 110642, DOI: 10.1016/j.est.2024.110642.

23 D. Cui, R. Wang, C. Qian, H. Shen, J. Xia, K. Sun, H. Liu, C. Guo, J. Li, F. Yu and W. Bao, *Materials*, 2023, **16**(4), 1430, DOI: 10.3390/ma16041430.

24 R. Alcántara, C. Pérez-Vicente, P. Lavela, J. L. Tirado, A. Medina and R. Stoyanova, *Materials*, 2023, **16**(21), 6970, DOI: 10.3390/ma16216970.

25 E. S. Goda, S. Lee, M. Sohail and K. R. Yoon, *J. Energy Chem.*, 2020, **50**, 206–229, DOI: 10.1016/j.jechem.2020.03.031.

26 D. Zhang, Z. Yang, J. Zhang, H. Mao, J. Yang and Y. Qian, *J. Power Sources*, 2018, **399**, 1–7, DOI: 10.1016/j.jpowsour.2018.07.084.

27 B. Wang, Y. Han, X. Wang, N. Bahlawane, H. Pan, M. Yan and Y. Jiang, *iScience*, 2018, **3**, 110–133, DOI: 10.1016/j.isci.2018.04.008.

28 X. Wu, M. Sun, S. Guo, J. Qian, Y. Liu, Y. Cao, X. Ai and H. Yang, *ChemNanoMat*, 2015, **1**(3), 188–193, DOI: 10.1002/cnma.201500021.

29 K. Lu, B. Song, X. Gao, H. Dai, J. Zhang and H. Ma, *J. Power Sources*, 2016, **303**, 347–353, DOI: 10.1016/j.jpowsour.2015.11.031.

30 F. Zhao, Y. Wang, X. Xu, Y. Liu, R. Song, G. Lu and Y. Li, *ACS Appl. Mater. Interfaces*, 2014, **6**(14), 11007–11012, DOI: 10.1021/am503375h.

31 A. Khan, M. Shahid, A. Inayat, S. M. Abbas, S. Peng, M. A. Mansoor, T. Nisar, V. Wagner and A. Haider, *J. Alloys Compd.*, 2023, **964**, 171303, DOI: 10.1016/j.jallcom.2023.171303.

32 M. Ciabocco, M. Berrettoni, S. Zamponi and J. A. Cox, *J. Solid State Electrochem.*, 2016, **20**, 1323–1329, DOI: 10.1007/s10008-016-3123-9.

33 H. Matsuoka, O. Tomita, H. Tabe, H. Suzuki, Y. Yamada and R. Abe, *J. Photochem. Photobiol., A*, 2022, **426**, 113753, DOI: 10.1016/j.jphotochem.2021.113753.

34 O. Calixto-Lozada, J. Vazquez-Samperio, E. Córdoba-Tuta, E. Reguera and P. Acevedo-Peña, *Solid State Sci.*, 2021, **116**, 106603, DOI: 10.1016/j.solidstatesciences.2021.106603.

35 M. Pasta, R. Y. Wang, R. Ruffo, R. Qiao, H. W. Lee, B. Shyam, M. Guo, Y. Wang, L. A. Wray, W. Yang, M. F. Toney and Y. Cui, *J. Mater. Chem. A*, 2016, **4**, 4211–4223, DOI: 10.1039/C5TA10571D.

36 Y. Qiu, Y. Lin, H. Yang and L. Wang, *J. Alloys Compd.*, 2019, **806**, 1315–1322, DOI: 10.1016/j.jallcom.2019.07.253.

37 Z. Zhang, J. G. Wang and B. Wei, *Nanomaterials*, 2017, **7**(8), 228, DOI: 10.3390/nano7080228.

38 L. Zhang, P. Jia, Z. Guo, Q. Cai, Z. Li, X. Zhu, R. Song, H. Yao and Z. Li, *J. Colloid Interface Sci.*, 2023, **646**, 78–88, DOI: 10.1016/j.jcis.2023.05.036.

39 D. L. Muhammad Fayaz, X. Liu, B. Chen, C. Wen, W. Lai, Z. Wang, Y. Chen and Y. Chen, *J. Energy Storage*, 2024, **98**, 112999, DOI: 10.1016/j.est.2024.112999.

40 R. D. Rodriguez, S. Shchadenko, G. Murastov, A. Lipovka, M. Fatkullin, I. Petrov, T. H. Tran, A. Khalelov, M. Saqib, N. E. Villa, V. Bogoslovskiy, Y. Wang, C. G. Hu, A. Zinovyev, W. Sheng, J. J. Chen, I. Amin and E. Sheremet, *Adv. Funct. Mater.*, 2021, **31**(17), 2008818, DOI: 10.1002/adfm.202008818.

41 M. Kaneva, A. Levshakova, I. Tumkin, M. Fatkullin, E. Gurevich, A. Manshina, R. D. Rodriguez and E. Khairullina, *Microchem. J.*, 2024, **204**, 111106, DOI: 10.1016/j.microc.2024.111106.

42 V. Tolstoy, M. Kaneva, N. Fedotova and A. Levshakova, *Ceram. Int.*, 2020, **46**(12), 20122–20128, DOI: 10.1016/j.ceramint.2020.05.087.

43 A. A. Lobinsky and M. V. Kaneva, *Nanosyst. Phys. Chem. Math.*, 2020, **11**(5), 608–614, DOI: 10.17586/2220-8054-2020-11-5-608-614.

44 V. P. Tolstoy, A. A. Lobinsky and M. V. Kaneva, *J. Mol. Liq.*, 2019, **282**(19), 32–38, DOI: 10.1016/j.molliq.2019.02.067.

45 Y. Borodaenko, S. Syubaev, E. Khairullina, I. Tumkin, S. Gurbatov, A. Mironenko, E. Mitsai, A. Zhizhchenko, E. Modin, E. L. Gurevich and A. A. Kuchmizhak, *Adv. Opt. Mater.*, 2022, **10**(21), 2201094, DOI: 10.1002/adom.202201094.

46 A. Lipovka, A. Garcia, E. Abyzova, M. Fatkullin, Z. Song, Y. Li, R. Wang, R. D. Rodriguez and E. Sheremet, *Adv. Opt. Mater.*, 2024, **12**(17), 2303194, DOI: 10.1002/adom.202303194.

47 E. M. Khairullina, I. I. Tumkin, D. D. Stupin, A. V. Smikhovskaia, A. S. Mereshchenko, A. I. Lihachev, A. V. Vasin, M. N. Ryazantsev and M. S. Panov, *ACS Omega*, 2021, **6**(28), 18099–18109, DOI: 10.1021/acsomega.1c01880.

48 A. Povolotckaia, D. Pankin, Y. Petrov, A. Vasileva, I. Kolesnikov, G. Sarau, S. Christiansen, G. Leuchs and A. Manshina, *J. Mater. Sci.*, 2019, **54**, 8177–8186, DOI: 10.1007/s10853-019-03478-9.

49 G. V. Murastov, A. A. Lipovka, M. I. Fatkullin, R. D. Rodriguez and E. S. Sheremet, *Phys. Usp.*, 2023, **66**, 1105–1133, DOI: 10.3367/UFNe.2022.12.039291.

50 M. Fatkullin, R. D. Rodriguez, I. Petrov, N. E. Villa, A. Lipovka, M. Gridina, G. Murastov, A. Chernova, E. Plotnikov, A. Averkiev, D. Cheshev, O. Semyonov, F. Gubarev, K. Brazovskiy, W. Sheng, I. Amin, J. Liu, X. Jia and E. Sheremet, *Nanomaterials*, 2023, **13**(5), 923, DOI: 10.3390/nano13050923.

51 E. S. R. D. Rodriguez, G. V. Murastov, A. Lipovka, M. I. Fatkullin, O. Nozdrina, S. K. Pavlov, P. S. Postnikov, M. M. Chehimi and J.-J. Chen, *Carbon*, 2019, **151**, 148–155, DOI: 10.1016/j.carbon.2019.05.049.

52 R. D. Rodriguez, M. Fatkullin, A. Garcia, I. Petrov, A. Averkiev, A. Lipovka, L. Lu, S. Shchadenko, R. Wang, J. Sun, Q. Li, X. Jia, C. Cheng, O. Kanoun and E. Sheremet, *Adv. Mater.*, 2022, **34**(43), 2206877, DOI: 10.1002/adma.202206877.

53 E. M. Khairullina, K. Ratautas, M. S. Panov, V. S. Andriianov, S. Mickus, A. A. Manshina, G. Račiukaitis and I. I. Tumkin, *Microchim. Acta*, 2022, **189**(7), 259, DOI: 10.1007/s00604-022-05347-w.

54 S. K. Sinha, P. Ghosh, S. Jain, S. Maiti, S. A. Al-Thabati, A. A. Alshehri, M. Mokhtar and D. Maiti, *Chem. Soc. Rev.*, 2023, **52**, 7461–7503, DOI: 10.1039/D3CS00282A.

55 B. D. Boruah, A. Maji and A. Misra, *ACS Appl. Mater. Interfaces*, 2018, **10**, 15864–15872, DOI: 10.1021/acsami.8b02660.

56 M. G. Say, C. J. Brett, J. Edberg, S. V. Roth, L. D. Söderberg, I. Engquist and M. Berggren, *ACS Appl. Mater. Interfaces*, 2022, **14**(50), 55850–55863, DOI: 10.1021/acsami.2c15514.

57 L. Wang, Y. Ding, Z. Xu, J. Li, Y. Guan, L. Yang, H. Gu and H. Fang, *Energy Storage Mater.*, 2024, **65**, 103132, DOI: 10.1016/j.ensm.2023.103132.

58 H. Wang, L. Tian, X. Zhao, M. Ali, H. Feng, S. Han, Z. Xing, S. Kumar and J. Ding, *J. Alloys Compd.*, 2023, **960**, 170835, DOI: 10.1016/j.jallcom.2023.170835.

59 N. Kurra, S. Uzun, G. Valurouthu and Y. Gogotsi, *Energy Storage Mater.*, 2021, **39**, 347–353, DOI: 10.1016/j.ensm.2021.04.037.

60 X. Yin, H. Li, R. Yuan, L. Zhang and J. Lu, *Sci. China Mater.*, 2020, **63**, 739–747, DOI: 10.1007/s40843-019-1251-8.

61 Z. Song, W. Liu, Q. Yuan, Q. Zhou, G. Liu and Z. Zhao, *J. Mater. Sci. Mater. Electron.*, 2018, **29**, 14897–14905, DOI: 10.1007/s10854-018-9628-5.

62 K. Krishnamoorthy, P. Pazhamalai, S. Sahoo, J. H. Lim, K. H. Choi and S. J. Kim, *ChemElectroChem*, 2017, **4**, 3302–3308, DOI: 10.1002/celc.201700690.

63 N. K. Alam Venugopal and J. Joseph, *J. Power Sources*, 2016, **305**, 249–258, DOI: 10.1016/j.jpowsour.2015.11.088.

64 S. J. Reddy, A. Dostal and F. Scholz, *J. Electroanal. Chem.*, 1996, **403**, 209–212, DOI: 10.1016/0022-0728(95)04380-2.

65 A. Levshakova, M. Kaneva, E. Borisov, M. Panov, A. Shmalko, N. Nedelko, A. S. Mereshchenko, M. Skripkin, A. Manshina and E. Khairullina, *Materials*, 2023, **16**(22), 7225, DOI: 10.3390/ma16227225.

66 N. A. Mohd Zaid and N. H. Idris, *Sci. Rep.*, 2016, **6**, 32082, DOI: 10.1038/srep32082.

67 S. Srivastava, K. Jain, V. N. Singh, S. Singh, N. Vijayan, N. Dilawar, G. Gupta and T. D. Senguttuvan, *Nanotechnology*, 2012, **23**(20), 205501, DOI: 10.1088/0957-4484/23/20/205501.

68 R. Mažeikiene, G. Niaura and A. Malinauskas, *J. Electroanal. Chem.*, 2014, **719**, 60–71, DOI: 10.1016/j.jelechem.2014.02.012.

69 X. Wang, B. Wang, Y. Tang, B. Bin Xu, C. Liang, M. Yan and Y. Jiang, *J. Mater. Chem. A*, 2020, **8**, 3222–3227, DOI: 10.1039/C9TA12376H.

70 A. Jorio and A. G. Souza Filho, *Annu. Rev. Mater. Res.*, 2016, **46**, 357–382, DOI: 10.1146/annurev-matsci-070115-032140.

71 C. L. C. Carvalho, A. T. B. Silva, R. A. S. Luz, G. M. B. Castro, C. Da Luz Lima, V. R. Mastelaro, R. R. Da Silva, O. N. Oliveira

and W. Cantanhêde, *ACS Appl. Nano Mater.*, 2018, **1**, 4283–4293, DOI: 10.1021/acsanm.8b01106.

72 J. Choi, J. Lee, J. Lim, S. Park and Y. Piao, *J. Alloys Compd.*, 2022, **914**, 165365, DOI: 10.1016/j.jallcom.2022.165365.

73 Y. Xu, Y. Du, Z. Yi, Z. Zhang, C. Lai, J. Liao and X. Zhou, *J. Energy Chem.*, 2021, **58**, 593–601, DOI: 10.1016/j.jechem.2020.10.039.

74 P. Xiong, G. Zeng, L. Zeng and M. Wei, *Dalt. Trans.*, 2015, **44**, 16746–16751, DOI: 10.1039/C5DT03030G.

75 S. J. Gerber and E. Erasmus, *Mater. Chem. Phys.*, 2018, **203**, 73–81, DOI: 10.1016/j.matchemphys.2017.09.029.

76 D. Sun, X. Wang and M. Qu, *Materials*, 2022, **15**(13), 4705, DOI: 10.3390/ma15134705.

77 L. Wang, Y. Lu, J. Liu, M. Xu, J. Cheng, D. Zhang and J. B. Goodenough, *Angew. Chem., Int. Ed.*, 2013, **52**(7), 1964–1967, DOI: 10.1002/anie.201206854.

78 J. Ge, L. Fan, A. M. Rao, J. Zhou and B. Lu, *Nat. Sustain.*, 2022, **5**, 225–234, DOI: 10.1038/s41893-021-00810-7.

79 E. Lee, S. Seong, H. W. Kim, D. H. Kim, N. Thakur, S. M. Yusuf, B. Kim, B. I. Min, Y. Kim, J. Y. Kim, F. M. F. De Groot and J. S. Kang, *Phys. Rev. B*, 2017, **96**, 195120, DOI: 10.1103/PhysRevB.96.195120.

80 Q. Ma, R. Dong, H. Liu, A. Zhu, L. Qiao, Y. Ma, J. Wang, J. Xie and J. Pan, *J. Alloys Compd.*, 2020, **820**, 153438, DOI: 10.1016/j.jallcom.2019.153438.

81 A. M. Vinu Mohan, G. Rambabu, K. K. Aswini and V. M. Biju, *Thin Solid Films*, 2014, **565**, 207–214, DOI: 10.1016/j.tsf.2014.06.018.

82 Y. Lin, L. Zhang, Y. Xiong, T. Wei and Z. Fan, *Energy Environ. Mater.*, 2020, **3**, 323–345, DOI: 10.1002/eem2.12096.

83 M. Antuch, Y. Matos-Peralta, D. Llanes, F. Echevarría, J. Rodríguez-Hernández, M. H. Marin, A. M. Díaz-García and L. Reguera, *ChemElectroChem*, 2019, **6**(5), 1567–1573, DOI: 10.1002/celc.201900190.

84 Y. Chen, R. C. Zhou, Y. H. Wan, J. W. Hao, H. R. You, X. M. Liu and H. Yang, *J. Electroanal. Chem.*, 2021, **887**, 115151, DOI: 10.1016/j.jelechem.2021.115151.

85 X. Zhao, D. He and B. You, *Mater. Today Sustain.*, 2022, **17**, 100096, DOI: 10.1016/j.mtsust.2021.100096.

86 B. Pandit, B. R. Sankapal and P. M. Koinkar, *Sci. Rep.*, 2019, **9**, 5892, DOI: 10.1038/s41598-019-42301-y.

87 M. Rajkumar, C. T. Hsu, T. H. Wu, M. G. Chen and C. C. Hu, *Prog. Nat. Sci. Mater. Int.*, 2015, **25**(6), 527–544, DOI: 10.1016/j.pnsc.2015.11.012.

88 V. Ravichandran, S. Shital Nardekar, D. Kesavan, J. P. Das, V. Elumalai and S. J. Kim, *Chem. Eng. J.*, 2024, **482**, 148822, DOI: 10.1016/j.cej.2024.148822.